Strikingly different neurotransmitter release strategies in dopaminergic subclasses

Ana Dorrego-Rivas[1*#], Darren J. Byrne[1*], Yunyi Liu[1], Menghon Cheah[1], Ceren Arslan[1], Marcela Lipovsek[1,2], Marc C. Ford[1], and Matthew S. Grubb[1#]

[1]Centre for Developmental Neurobiology, Institute of Psychiatry, Psychology and Neuroscience (IoPPN), King's College London, London, UK

[2]Current address: Ear Institute, University College London, London, UK

*These authors contributed equally to this work

[#]Corresponding authors: ana.dorrego-rivas@kcl.ac.uk , matthew.grubb@kcl.ac.uk

Abstract

Neuronal function is intimately tied to axodendritic polarity. Neurotransmitter release, for example, is usually the role of the axon. There are widespread exceptions to this rule, however, including many mammalian neuronal types that can release neurotransmitter from their dendrites. In the mouse olfactory bulb, closely related subclasses of dopaminergic interneuron differ markedly in their polarity, with one subtype lacking an axon entirely. These axon-bearing and anaxonic dopaminergic subclasses have distinct developmental profiles and sensory responses, but how their fundamental polarity differences translate to functional outputs remains entirely unknown. Here, we provide anatomical evidence for distinct neurotransmitter release strategies among these closely related dopaminergic subtypes: anaxonic cells release from their dendrites, while axon-bearing neurons release exclusively from their intermittently myelinated axon. These structural differences are linked to a clear functional distinction: anaxonic, but not axon-bearing dopaminergic neurons are capable of self-inhibition. Our findings suggest that variations in polarity can produce striking distinctions in neuronal outputs, and that even closely related neuronal subclasses may play entirely separate roles in sensory information processing.

Introduction

Neurons are one of the most striking examples of cell polarisation. Most neurons have canonical axodendritic polarity, defined by the presence of a somatodendritic domain and a single axon (Banker, 2018). The morphological and molecular specialisation of these distinct compartments gives them unique functional properties, with dendrites usually receiving most synaptic inputs, and axons sending outputs to other neurons by releasing neurotransmitters. However, exceptions to this neuronal polarity dogma are common. In the mammalian brain, there are neurons – including midbrain dopaminergic cells (Pucak and Grace, 1994; Falkenburger et al., 2001) and cortical bitufted cells (Zilberter et al., 1999) – that release neurotransmitter from their dendrites. There are also neurons – including retinal amacrine cells (Wu et al., 2011; Goaillard et al., 2020) – that lack

canonical axons altogether. A remarkable hub for such unconventional neuronal polarity is the olfactory bulb (OB), the first part of the brain that processes information about the sense of smell. Dendritic release of neurotransmitters is a widespread phenomenon in the OB, even in projection neurons and other cells with classically defined axodendritic polarity (Schoppa and Urban, 2003; Hayar et al., 2004; Imamura et al., 2020). In addition, non-canonical polarity is extremely common in the OB, where almost all GABAergic interneurons lack an axon entirely (Tufo et al., 2022).

Neuronal polarity in the OB can be completely different even in closely related neuronal subtypes. In the glomerular layer, a major class of interneurons releases both dopamine and GABA in order to modulate neurotransmitter release from olfactory sensory neuron terminals and to regulate downstream processing in local circuits (Wachowiak and Cohen, 1999; Berkowicz and Trombley, 2000; Borisovska et al., 2013, Liu et al., 2013; Banerjee et al., 2015; Vaaga et al., 2017). We recently found that these dopaminergic (DA) neurons can be classified into two subtypes depending on a binary morphological distinction: the presence or absence of an axon. This fundamental divergence in polarity is correlated with different excitability profiles and odour response properties (Chand et al., 2015; Galliano et al., 2018; Lau et al., 2024). However, the specific function of these two neuron subtypes within OB glomerular networks is not fully understood. A crucial outstanding question is how the structural differences in these two neuron subtypes translate into strategies for influencing bulbar circuits via neurotransmitter release.

Anaxonic DA neurons only have a soma and dendrites (Chand et al., 2015; Galliano et al., 2018) making these the sole available domains for neurotransmitter release. Indeed, dendritic presynaptic structures are present in DA neurons (Kiyokage et al., 2017), and are associated with these cells' functional ability to self-inhibit via local GABA release (Smith and Jahr, 2002; Murphy et al., 2005; Maher and Westbrook, 2008). On the other hand, axon-bearing DA neurons are known to be the sole source of long-range interglomerular connections in the OB (Kosaka and Kosaka, 2008), with functional studies showing that these cells release neurotransmitters over these long-distance axonal projections (Liu et al., 2013; Whitesell et al., 2013; Banerjee et al., 2015). However, in a brain region where dendritic release is the norm rather than the exception, what remains unknown is whether axon-bearing DAs combine this distal, *inter*glomerular signalling with local, *intra*glomerular inhibition via release from their dendrites. Answering this question has important implications for how information is processed in early olfactory circuits.

Here, we provide anatomical evidence showing that axon-bearing OB DA neurons have axons with neurotransmitter release sites, while their dendrites lack these sites almost entirely. On the other hand, we found that all anaxonic DA neurons have release sites on their dendrites. These structural differences are associated with a striking functional distinction: while all anaxonic neurons can self-inhibit, there is an almost total absence of self-inhibition responses in the axon-bearing subpopulation. This polarity-based dichotomy suggests that even these closely related interneuron subtypes may play entirely separate roles in the processing of sensory information.

Results

Labelling putative presynaptic structures in individual olfactory bulb dopaminergic neurons

We first developed a structural approach for labelling putative presynaptic sites in individual OB DA neurons. We observed that synaptophysin, a membrane protein located in vesicles at the presynapse, is expressed in OB DA cells at both the mRNA (**Figure 1A**) and protein (**Figure 1B**) levels. Given the high synaptic density and complexity of OB glomeruli, it is not possible to reliably assign

specific synaptophysin label to individual DA neurons using widespread staining of endogenous protein. We therefore chose a sparse labelling approach based on the injection of an AAV-DJ-hSyn-FLEx-mGFP-T2A-Synaptophysin-mRuby construct (Beier et al., 2015; Kathe, et al., 2022). This vector allows the expression in individual cre-expressing cells of a membrane-bound GFP for cell morphology, and fluorophore-tagged full-length synaptophysin for the visualisation of putative presynaptic puncta. There is strong evidence showing that the overexpression of fluorophore-tagged synaptophysin is functionally benign (Granseth et al., 2006; Li and Tsien, 2012).

We performed *in utero* injections in embryonic day 14 (E14) vGAT (vesicular GABA transporter)-cre mice. This timepoint ensures the effective labelling of axon-bearing and anaxonic DA neurons, since both cell types are generated during embryonic development. (**Figure 1C**, Batista-Brito et al., 2008; Galliano et al., 2018). Dopaminergic neurons were then identified via immunostaining against tyrosine hydroxylase (TH), the rate-limiting enzyme in the synthesis of dopamine (Galliano et al., 2018). We were able to detect well-defined synaptophysin-mRuby puncta along the processes of TH+ GFP+ neurons (**Figure 1D**).

To assess whether this method labels reliable presynaptic release sites in DA neurons, we co-stained the injected tissue against vGAT and observed high co-localisation between endogenous vGAT and mRuby label (**Figure 1E**; 39/53 = 74 % synaptophysin-mRuby puncta co-localised with vGAT; n = 9 cells from N = 4 mice). These results demonstrate that a large proportion of synaptophysin-mRuby puncta are likely to reflect putative presynaptic release sites in OB DA neurons.

Figure 1

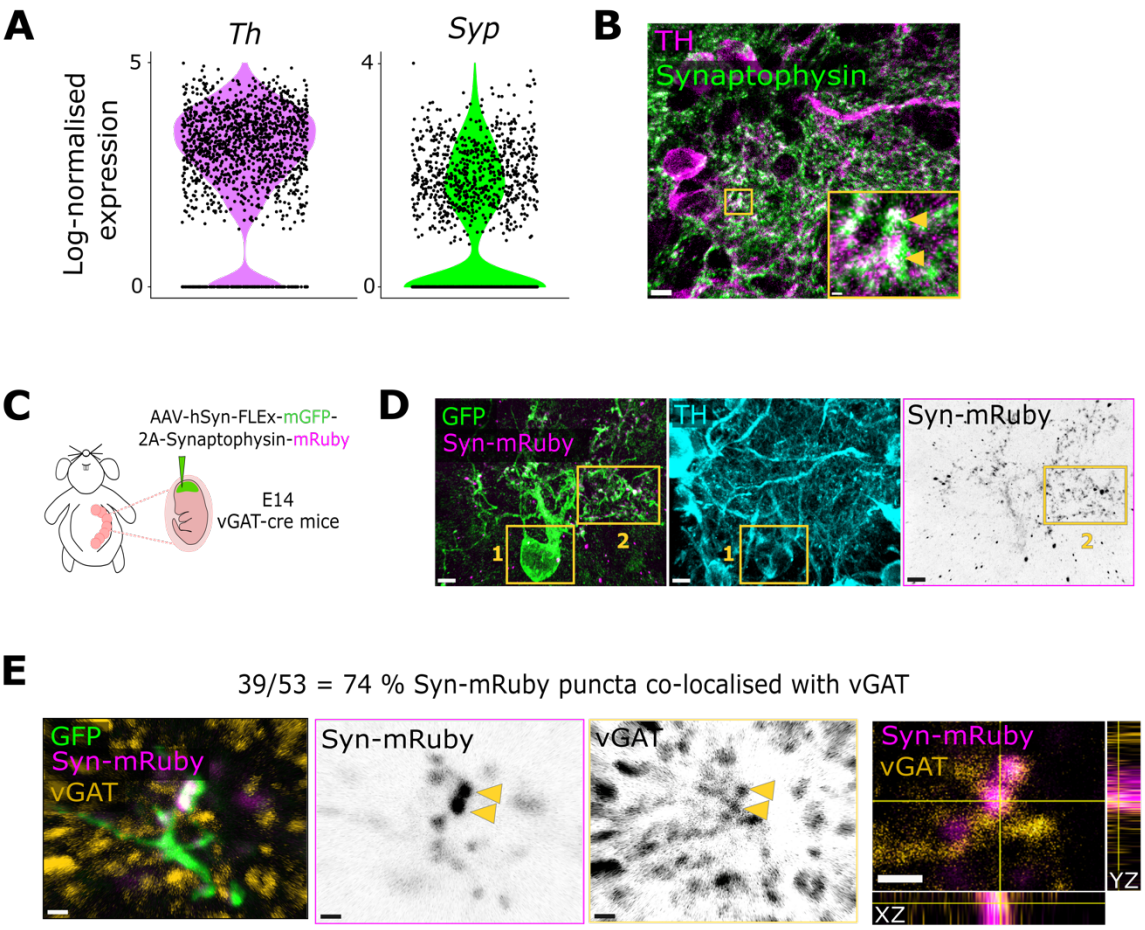

103 **Figure 1**. **Labelling putative presynaptic structures in individual olfactory bulb dopaminergic neurons. (A)**
104 Log_2-normalised expression of *Th* and *Syp* mRNA in DA neurons from single cell RNA sequencing data (Brann et
105 al., 2020). **(B)** Example snapshot of a 3D confocal stack of endogenous immunostaining for synaptophysin
106 (green) and TH (magenta) in the glomerular layer of the OB. Yellow arrowheads point to small clusters where
107 TH and synaptophysin co-localise. Scalebars: 5 μm (main) and 0.5 μm (inset). **(C)** Strategy to label putative
108 presynaptic release sites in individual DA neurons. **(D)** Example snapshot of a 3D confocal stack of a
109 successfully labelled DA cell. Inset 1 reveals the TH+ dopaminergic identity of the neuron (cyan), and inset 2
110 highlights the Syn-mRuby puncta (magenta, black). Scalebars, 5 μm. **(E)** Example snapshot of a 3D confocal
111 stack of a GFP+ (green), Syn-mRuby+ (magenta, black) neuronal process co-stained with vGAT (orange, black).
112 Yellow arrowheads indicate examples where Syn-mRuby and vGAT puncta co-localise. The last panel shows the
113 orthogonal views of the bottom puncta. Scalebars, 1 μm.

114

115 **Anaxonic DA neurons have dendritic neurotransmitter release sites**

116 Given that anaxonic DA neurons lack an axon, and are known to release both GABA and dopamine,
117 to be able to release neurotransmitter they must have presynaptic release sites on their dendrites.
118 We identified this neuronal subtype in our population of GFP+/TH+ neurons by the lack of the
119 proximal axonal marker TRIM46 (**Figure 2A**, van Beuningen et al., 2015; Galliano et al., 2018).

Figure 2

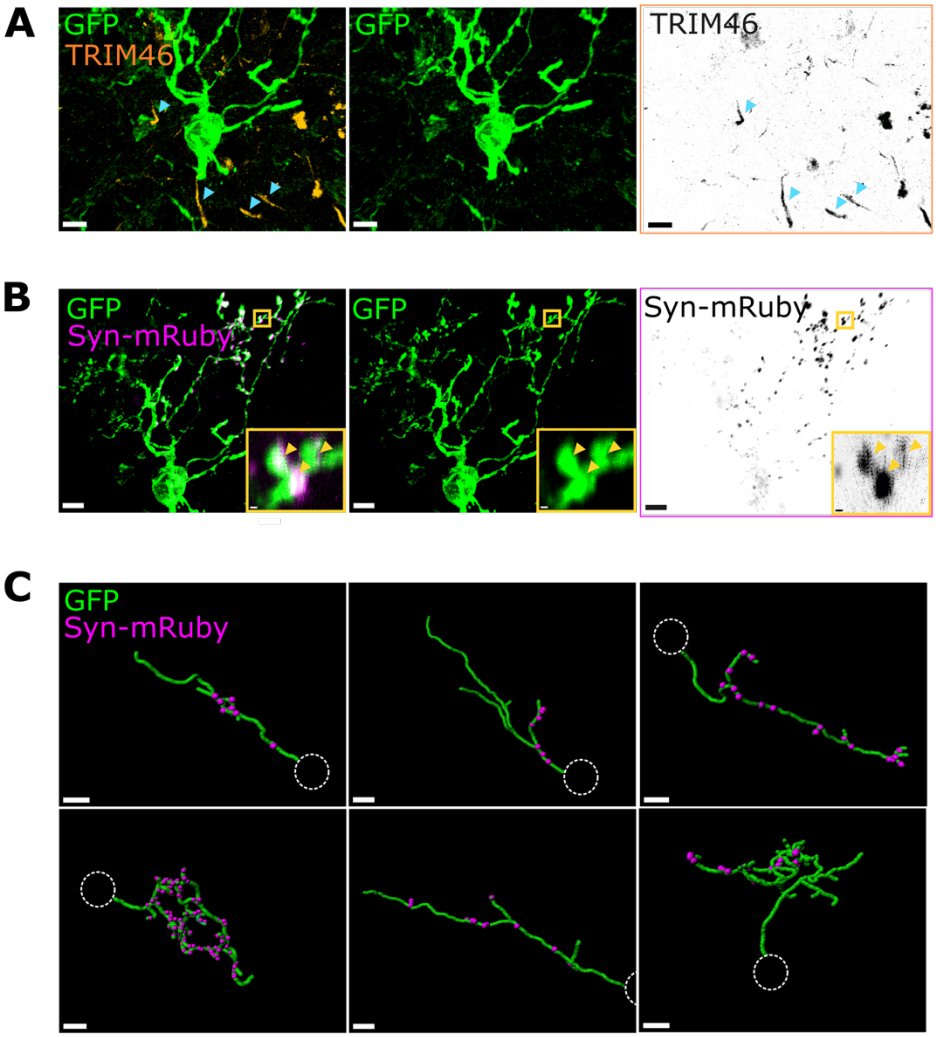

Figure 2. **Anaxonic DA neurons have dendritic neurotransmitter release sites. (A)** Example snapshot of a 3D confocal stack of a TRIM46- anaxonic DA neuron. Blue arrowheads point to examples of other TRIM46+ AISs (orange, black) in the same region which do not co-localise with this neuron's GFP signal. Scalebars, 5 μm. **(B)** Snapshot of the same neuron in (A) showing Synaptophysin-mRuby Puncta (magenta, black) on the dendrites. Yellow inset highlights a region of the neuron with multiple mRuby+ puncta within the GFP+ (green) processes (yellow arrows). Scalebars, 5 μm and 0.5 μm. **(C)** Example snapshots from 3D dendritic reconstructions (green, GFP) and presynaptic puncta detection (magenta, Syn-mRuby) of anaxonic DA neurons. Note: these are not full dendritic reconstructions, but example dendrites. Dotted white circle represents the soma location. Scalebars, 5 μm.

As predicted, we found that all anaxonic neurons had synaptophysin-mRuby puncta in their dendrites (**Figure 2B, C;** n=9 anaxonic DA cells from N=4 mice). The thin slices necessary for puncta detection precluded any comprehensive analysis of dendritic morphology or synaptic distributions. Nevertheless, we saw no consistent evidence for spatial patterns, clusters, or privileged branches; instead, puncta were distributed throughout each cell's dendritic arbour (**Figure 2C**). These results provide anatomical evidence for the presence of dendritic neurotransmitter release sites in anaxonic DA neurons.

Axonic DA neurons have release sites on their intermittently myelinated axons, but not on their dendrites

Long-range GABA release has been functionally demonstrated in dopaminergic neurons (Liu et al., 2013; Whitesell et al., 2013; Banerjee et al., 2015), strongly suggesting that axon-bearing DA neurons have axonal release sites. It was not possible to follow TRIM46+ DA axons for long distances from the soma in thin brain slices, so instead we used the distal axon marker myelin basic protein (MBP). In the first description of myelination in this cell type, we found that DA axons are myelinated in an intermittent pattern, a common trait in other brain regions (**Figure 3A**, Tomassy et al., 2014). Using MBP as indicator of axon identity, we were then able to locate synaptophysin-mRuby puncta in unmyelinated sections of GFP+ TH+ axons (**Figure 3B;** n=2 axon-bearing DA cells from N=1 mouse). As predicted, axon-bearing DA neurons therefore have putative presynaptic release sites on their axons.

Most neurons with canonical axodendritic polarity in the olfactory bulb release neurotransmitters from both axons and dendrites (Castro and Urban, 2009). To assess if this scenario also holds true for DA axon-bearing cells, we explored the dendritic localisation of synaptophysin-mRuby-labelled presynaptic release sites in GFP+ neurons with clear TRIM46+ proximal axonal domains (**Figure 3C**). As expected, these axon-bearing OB DA cells had larger somas than their anaxonic neighbours (**Figure 3D**; soma area: 110.3 ± 7.72 μm^2 for axon-bearing DA cells, 61.99 ± 4.41 μm^2 for anaxonic DA neurons; n = 11 axon-bearing cells and n = 9 anaxonic neurons from N = 4 mice; unpaired t-test with Welch's correction, $p < 0.0001$). Given previous findings that axon-bearing DA cells have more widely ramified dendritic trees (Galliano et al., 2018), we ensured that our reconstructions of TRIM46-negative dendritic processes were equally extensive in both cell subtypes (maximum length of reconstructed dendrites: 67.64 ± 8.96 μm for axon-bearing DA cells, 74.88 ± 11.68 μm for anaxonic DA neurons; n = 11 axon-bearing cells and n = 9 anaxonic neurons from N = 4 mice; unpaired t-test with Welch's correction, $p = 0.6299$). We found that, unlike their anaxonic counterparts, almost all TRIM46+ neurons (10/11 cells from N = 4 mice, = 90.9 %) did not have any synaptophysin-mRuby puncta on their dendrites (**Figure 3E, F**; dendritic puncta density: 0.02 ± 0.02 $(\mu m)^{-1}$ for axon-bearing cells, 0.19 ± 0.04 $(\mu m)^{-1}$ for anaxonic neurons; n = 11 axon-bearing cells and n = 9 anaxonic neurons from N = 4 mice; Mann-Whitney test; $p = 0.0001$). We did find one single axon-bearing DA neuron

166 with apparent dendritic puncta; however, this cell had dramatically higher levels and unusual
167 patterns of expression as compared to all other GFP+ neurons (**Supplementary Figure 1**) and we
168 include it in our sample only through an abundance of caution. These findings provide a structural
169 basis for dendritic neurotransmitter release in anaxonic DA neurons, but not in the axon-bearing
170 population of DA neurons in the OB.

Figure 3

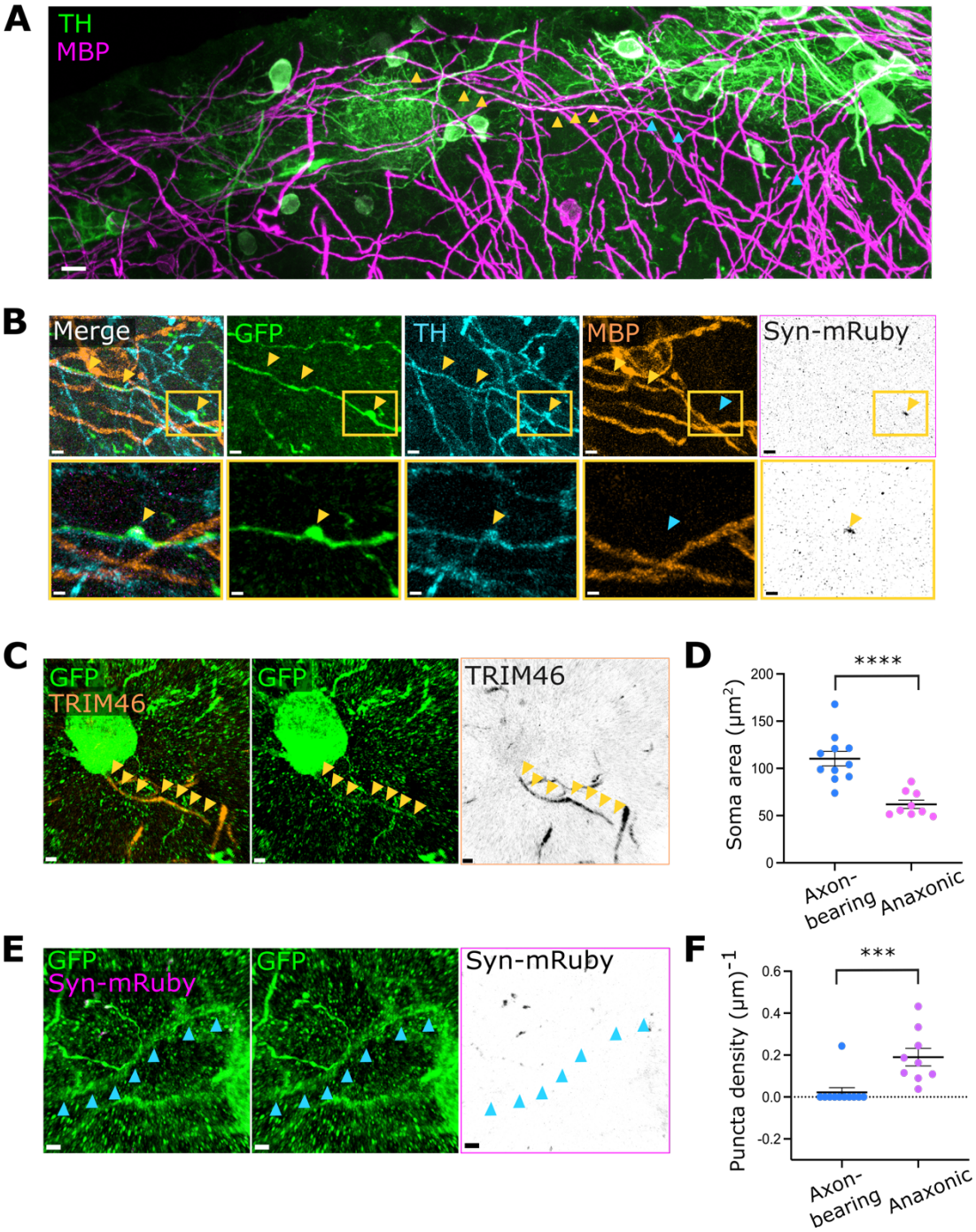

171 **Figure 3**. **Axon-bearing DA neurons have release sites on their intermittently myelinated axons, but not on**
172 **their dendrites. (A)** Stitching of individual confocal stacks processed for maximum intensity projections of OB
173 DA neurons co-stained with TH (green) and myelin basic protein (MBP, magenta). Yellow arrowheads point to
174 myelinated parts of the axon, blue arrowheads show unmyelinated areas. Scalebar, 10 µm. **(B)** Snapshot of a

3D confocal stack of a distal DA axon stained with GFP (green), TH (cyan), MBP (orange) and synaptophysin-mRuby (magenta, black). Yellow inset highlights the location of the presynaptic bouton. Yellow arrowheads point to co-localised regions, blue arrowheads show non-co-localisation. Scalebars, 2 μm and 1 μm. **(C)** Snapshot of a 3D confocal stack of an axon-bearing TRIM46+ DA neuron. Yellow arrowheads show co-localised staining for GFP (green) and TRIM46 (orange, black). Scalebars, 2 μm. **(D)** Soma area of axon-bearing and anaxonic DA neurons. Each dot shows one cell; lines show mean ± SEM; n = 11 axon-bearing cells and n = 9 anaxonic neurons from N = 4 mice; unpaired t-test with Welch's correction; ****, p <0.0001. **(E)** Snapshot of a 3D confocal stack of the same axon-bearing DA neuron showed in (C), co-stained with GFP (green) and synaptophysin-mRuby (magenta, black). Blue arrows show dendritic segments lacking mRuby label, despite the presence of clear mRuby+ puncta in neighbouring non-GFP+ processes. Scalebars, 2 μm. **(F)** Dendritic puncta density in axon-bearing and anaxonic DA neurons. All conventions as in D; n = 11 axon-bearing cells and n = 9 anaxonic neurons from N = 4 mice; Mann-Whitney's t-test; **, p = 0.0001.

Anaxonic DA neurons are capable of GABAergic self-inhibition

The fact that dendritic release sites are likely located near dendritic receptors (Kiyokage et al., 2017) might have the functional consequence that anaxonic DA cells can signal to themselves and influence their own activity. We found that OB DA neurons do not express DA receptors at the mRNA level (**Figure 4A**), making it unlikely that they could influence their own activity via DA signalling. However, GABAergic auto-evoked inhibition (AEI) or self-inhibition has been described in OB periglomerular cells in general, and in DA neurons in particular (Smith and Jahr, 2002; Murphy et al., 2005; Maher and Westbrook, 2008; Borisovska et al., 2013). In addition, we observed that the postsynaptic protein gephyrin can be in very close proximity to synaptophysin-mRuby puncta in the dendrites of anaxonic DA neurons (**Figure 4B**), suggesting that self-inhibition is possible in this specific cell subtype.

To address if anaxonic DA neurons can indeed self-inhibit, we used the DAT-tdT mouse line to specifically label DA neurons (Bäckman et al., 2006; Madisen et al., 2009; Galliano et al., 2018), and performed whole-cell patch clamp in tdT+ cells to evoke AEI responses. We identified the anaxonic DA population by their characteristic 'monophasic' phase-plane plot profile (**Figure 4C**; Galliano et al., 2018). After evoking transmitter release with transient depolarisation, we observed a prolonged inward current which was blocked by adding the GABA-A receptor antagonist gabazine at 10 μM (**Figure 4D;** AEI charge: 44.11 ± 6.02 pC; n = 31 cells from N = 18 mice). These data reveal that anaxonic DA neurons display AEI responses, consistent with the co-existence of presynaptic release sites and postsynaptic targets in the dendrites of these cells.

Although the AEI response is initiated by the depolarisation of the recorded anaxonic DA neuron, it has always been assumed, but not demonstrated, that the response is the direct result of GABA released from the same cell. However, given the presence of other GABAergic cells in local glomerular circuits (Kiyokage et al., 2017; for review see Tufo et al., 2022), there are other potential indirect ways in which depolarising a DA neuron might produce a GABA response in that same cell.

DA neurons in the OB release GABA and dopamine (Borisovska et al., 2013), and D1-like and D2-like dopamine receptors are expressed in the glomerular layer (Coronas et al., 1997). When we depolarise an anaxonic DA neuron to evoke neurotransmitter release, it is therefore possible that the dopamine that is co-released with GABA activates the dopamine receptors of neighbouring neurons, evoking secondary GABA release that then drives the AEI response in the recorded cell (**Figure 4E**). To rule out this possibility, we showed that the AEI response was unaffected by the application of D1-like and D2-like receptor antagonists (10 μM SFK 83566-hydrobromide and 10 μM

sulpiride, respectively; **Figure 4F, G**; AEI charge before blockers: 20.52 ± 1.93 pC , charge after blockers: 20.63 ± 2.59 pC; n = 3 cells from N = 3 mice; unpaired t-test with Welch's correction, p=0.71). These results show that the AEI response is not mediated by dopamine acting through other neurons.

Figure 4

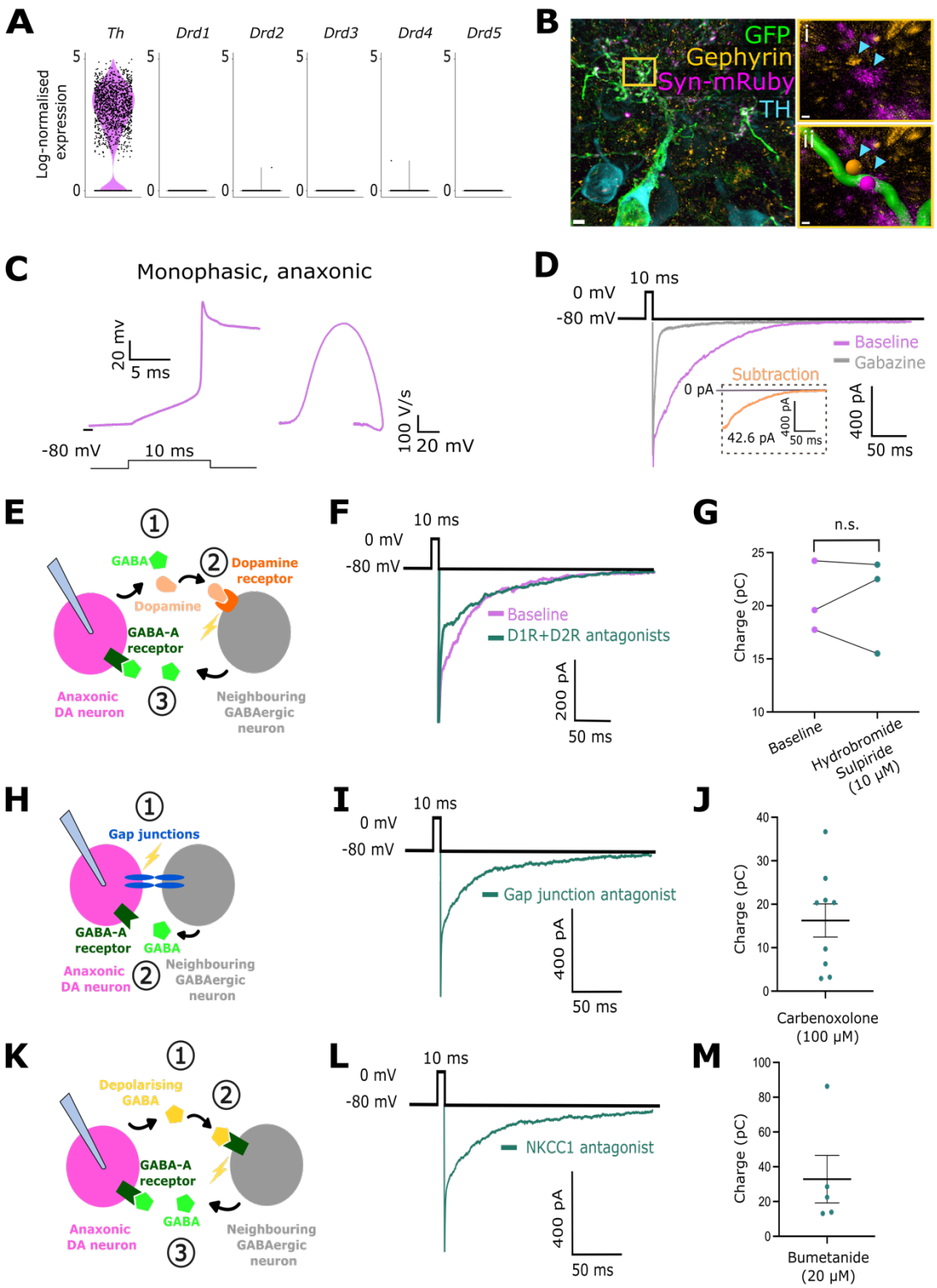

224 **Figure 4**. **Anaxonic DA neurons are capable of self-inhibition. (A)** Log_2-normalised expression (of *Th, Drd1,*
225 *Drd2, Drd3, Drd4* and *Drd5* mRNA in OB DA cells. **(B)** Snapshot of a 3D confocal stack of a virally labelled (GFP+,
226 green) anaxonic DA (TH+, cyan) neuron stained against gephyrin (orange) and synaptophysin-mRuby
227 (magenta). **i)** and **ii)** magnification of the boxed area; green shows reconstructed dendrite; blue arrowheads
228 point to two neighbouring puncta, one mRuby+ and one gephyrin+. Scalebars, 3 μm and 0.5 μm. **(C)** Example
229 trace of an action potential fired by a putative anaxonic DA neuron (left) and its monophasic phase-plane plot
230 profile (right). Note the prolonged repolarisation due to Cs-based internal solution. **(D)** Example traces of an
231 AEI response recorded before (magenta) and after (grey) the application of gabazine. The subtraction is shown
232 in the orange inset trace. **(E)** Schematic showing the potential involvement in the AEI response of neighbouring
233 GABAergic neurons activated by dopamine released from the patched DA cell. **(F)** Example traces of an AEI
234 response before (purple) and after (green) applying D1-like and D2-like receptor blockers (hydrobromide and
235 sulpiride, each at 10 μM). **(G)** AEI charge before (purple) and after (green) applying dopamine receptor
236 antagonists; n = 3 cells from N = 3 mice; unpaired t-test with Welch's correction: n.s., non-significant. **(H)**
237 Schematic showing the potential involvement in the AEI response of neighbouring GABAergic neurons
238 activated via gap junctions. **(I)** Example trace of an AEI response in the presence of the gap junction blocker
239 carbenoxolone at 100 μM. **(J)** AEI charge in the presence of carbenoxolone at 100 μM. Each dot shows one
240 cell; lines show mean ± SEM; n = 9 cells from N = 4 mice. **(K)** Schematic showing the potential involvement in
241 the AEI response of neighbouring GABAergic neurons activated by depolarising GABA released from the
242 patched cell. **(L)** Example trace of an AEI response in the presence of the NKCC1 channel blocker bumetanide
243 at 20 μM. **(M)** AEI charge in the presence of bumetanide at 20 μM. All conventions as in F; n = 5 cells from
244 N = 3 mice.

245

246 Glomerular neurons are electrically coupled via gap junctions (Schoppa and Westbrook, 2002;
247 Kosaka et al., 2005; Banerjee et al., 2015). To exclude the possibility that the electrical activation of
248 neighbouring, GABA-releasing neurons is mediating the AEI response (**Figure 4H**), we showed that
249 AEI was still present after gap junctions were pharmacologically blocked with 100 μM carbenoxolone
250 (**Figure 4I, J**; AEI charge after blockers: 16.27 ± 3.83 pC; n = 9 cells from N = 4 mice).

251 Finally, another source of activation of neighbouring GABA-releasing neurons could be GABA itself:
252 GABA can have depolarising effects on glomerular layer neurons (Parsa et al., 2015). To show that
253 the GABA released by the recorded neuron is not activating neighbouring GABA-releasing cells
254 (**Figure 4K**), we recorded strong AEI responses when depolarising GABA responses were prevented
255 in the presence of the Na-K-Cl cotransporter 1 (NKCC1) blocker bumetanide used at 20 μM (**Figure**
256 **4L, M**; AEI charge after blockers: 32.86 ± 13.66; n = 5 cells from N = 3 mice). Altogether, these data
257 robustly demonstrate that the AEI response in anaxonic DA neurons indicates true self-inhibition.

258

259 **Axon-bearing DA neurons do not self-inhibit**

260 We next wanted to assess whether axon-bearing DA neurons can self-inhibit. In light of our
261 anatomical data showing the presence of release sites exclusively on the distal axon, we predicted
262 that these cells do not exert synaptic inputs onto themselves. Using the same DAT-tdTomato mouse
263 line to label DA neurons, we identified tdT+ axon-bearing DA neurons by their characteristic
264 'biphasic' action potential waveform (**Figure 5A**, Galliano et al., 2018). As predicted, GABA-mediated
265 AEI currents were lacking in almost all axon-bearing DA neurons (**Figure 5B, C;** 8/9 cells from N = 5
266 mice, = 89 %; mean ± SEM AEI charge for axon-bearing neurons: 3.8 ± 2.8 pC; n = 9 cells from N = 5
267 mice; anaxonic cells: 44.11 ± 6.02 pC; n = 31 cells from N = 18 mice; Mann-Whitney test, $p < 0.0001$)
268 despite these neurons having functional GABA-A receptors as shown by the presence of prominent
269 gabazine-sensitive spontaneous IPSCs (**Figure 5D;** n = 9 axon-bearing neurons from N = 5 mice; n =

31 anaxonic cells from N = 18 mice). Even when we attempted to maximise AEI amplitude via a paired-pulse protocol (Bouhours et al., 2011) or prolonged depolarisation, we still saw no evidence of self-inhibition in this cell subtype (**Figure 5E, F;** AEI charge for single response: 5.4 ± 2.61 pC; n = 8 cells from N = 7 mice; AEI charge for paired response: 1.51 ± 2.91 pC; n = 8 cells from N = 7 mice; Wilcoxon matched-pairs signed rank test, p = 0.06. AEI charge for 10 ms response: 0.26 ± 0.21 pC, n = 7 cells from N = 6 mice; AEI charge for 100 ms response: 7.75 ± 7.51 pC; n = 7 cells from N = 6 mice; Wilcoxon matched-pairs signed rank test, p = 0.30). Axon-bearing DA neurons did produce a tail current in response to the AEI protocol; however, this was insensitive to gabazine and was instead abolished by adding the voltage-gated calcium channel blocker cadmium at 200 μM (**Figure 5G;** cadmium sensitive current: 24.1 ± 6.69 pC; n = 2 cells from N = 2 mice).

In conclusion, these findings provide both structural and functional evidence showing that anaxonic DA neurons in the OB can signal locally, even to the point of self-inhibition. In contrast, axon-bearing DA neurons can – unlike all other major cell types in this brain region – only release neurotransmitters distally from their axon.

Figure 5

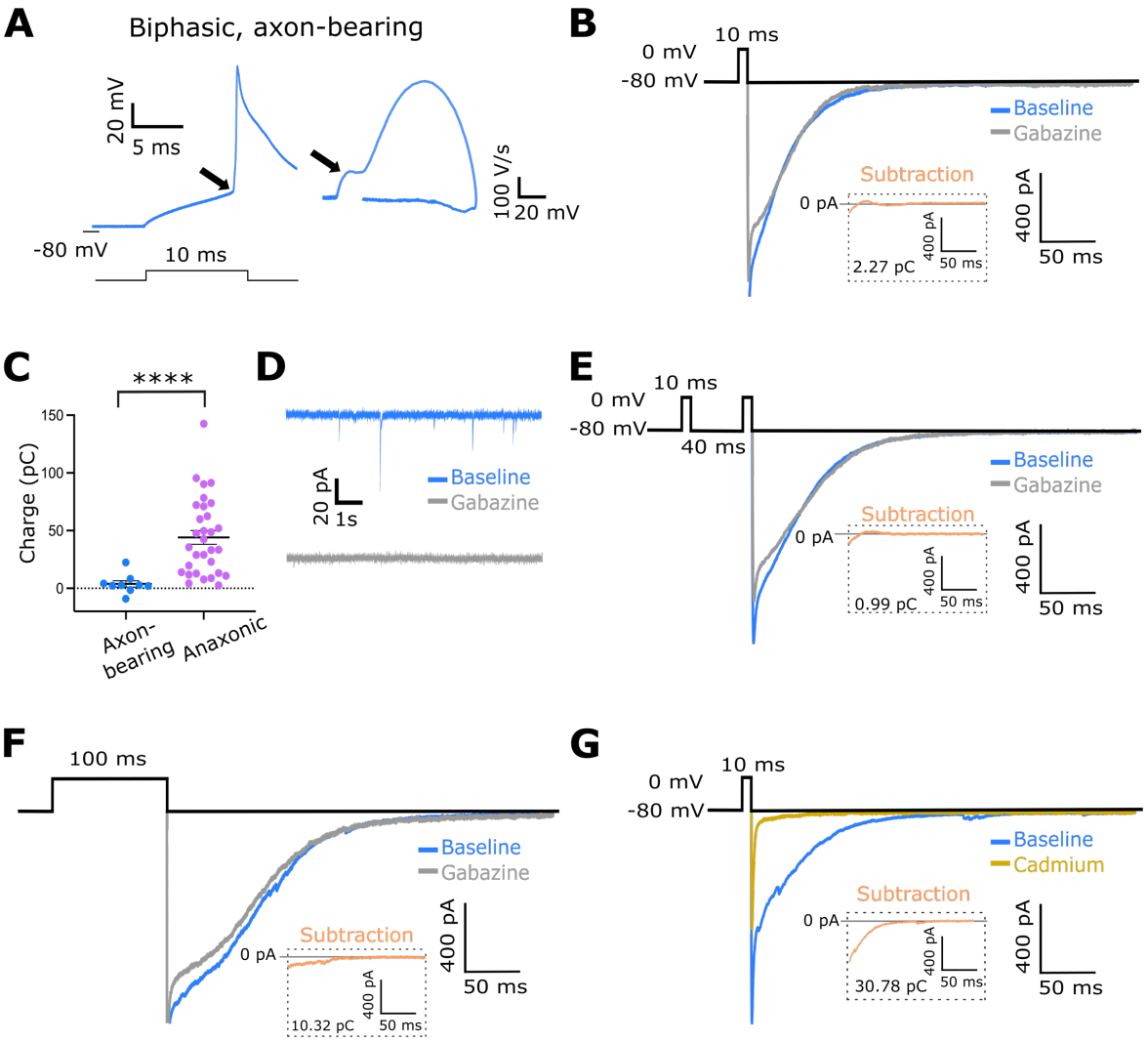

285 **Figure 5**. **Axon-bearing DA neurons do not self-inhibit. (A)** Example trace of an action potential fired by a
286 putative axon-bearing DA neuron (left) and its biphasic phase-plane plot profile (right). Arrows point to spike
287 onset kink (left) and initial segment bump (right). Note the prolonged repolarisation due to Cs-based internal
288 solution. **(B)** Example traces showing tail current responses in an axon-bearing DA neuron before (blue) and
289 after (grey) the application of gabazine. The subtraction is shown in the orange inset trace. **(C)** AEI charge in
290 axon-bearing and anaxonic DA neurons. Each dot shows one cell; lines show mean ± SEM; n = 9 axon-bearing
291 cells, n = 31 anaxonic cells from N = 18 mice; Mann-Whitney test; ****, $p < 0.0001$. **(D)** Example traces
292 showing spontaneous IPSCs in an axon-bearing DA neuron before (blue) and after (grey) the application of
293 gabazine. **(E), (F)** Example traces showing tail current responses in axon-bearing DA neurons before (blue) and
294 after (grey) the application of gabazine using a paired-pulse protocol **(E)** and prolonged depolarisation **(F)**.
295 Subtractions are shown in the orange inset traces. **(G)** Example traces showing that the tail current recorded in
296 axon-bearing DA neurons (blue) is blocked by cadmium (ocre). The subtraction is shown in the orange inset
297 trace.

298

299 ## Discussion

300 Our results show that different polarity-defined dopaminergic (DA) subtypes in the olfactory bulb
301 use distinct anatomical compartments for neurotransmitter release. While anaxonic DA neurons
302 release from the dendrites, axon-bearing DA cells release nearly exclusively from the axon. These
303 anatomical findings correlate strongly with different function: anaxonic DA neurons can self-inhibit,
304 but this ability is absent in almost all of the axon-bearing DA population.

305

306 **The link between neuronal polarity and neurotransmitter release**

307 Our anatomical data indicate that anaxonic DA neurons have release sites on their dendrites, while
308 the presynaptic sites of almost all the axon-bearing DA cells are located exclusively on their
309 intermittently myelinated axons. These findings are entirely consistent with previous descriptions of
310 release site localisation in similar OB cell types. Early ultrastructural work showed the absence of
311 release sites in the dendrites of axon-bearing neurons in the glomerular layer, defined
312 morphologically as 'short-axon cells' (Pinching and Powell, 1971). It was also shown that axon-
313 bearing DA neurons located in the external plexiform layer do not have dendritic release sites
314 (Liberia et al., 2012). In contrast, further ultrastructural work revealed the presence of release sites
315 in the dendrites of small DA periglomerular neurons, presumably anaxonic (Kiyokage et al., 2017).
316 Our results agree with all of these findings while specifically assigning different neurotransmitter
317 release strategies to axon-bearing and anaxonic DA neurons.

318 We have shown that anaxonic DA neurons use their only available anatomical compartment, the
319 dendrites, to release neurotransmitters. This paradigm of anaxonic structural and functional polarity
320 is unconventional but is found in other neuron types, including amacrine cells in the retina and OB
321 granule cells (Wu et al., 2011; Marshak, 2016; Nunes and Kuner, 2018). In fact, dendritic release is
322 not an uncommon phenomenon in the brain and is observed even in many axon-bearing neurons.
323 Dopaminergic neurons in the midbrain, for example, are one of the most studied examples of
324 dendritic release (Cheramy et al., 1981; Hikima et al., 2021). In the olfactory bulb, most neurons with
325 axodendritic polarity can release from both the axon and the dendrites, including mitral cells and
326 external tufted cells (Isaacson and Strowbridge, 1998; Schoppa and Urban, 2003; Hayar et al., 2004).
327 In this context, axon-bearing OB DA neurons are unique: they do not have dendritic release despite
328 their dopaminergic nature, and despite their identity as OB neurons with classic axodendritic
329 polarity.

330 OB DA neurons co-release both GABA and dopamine (Wachowiak and Cohen, 1999; Berkowicz and
331 Trombley, 2000; Borisovska et al., 2013, Liu et al., 2013; Vaaga et al., 2017 Banerjee et al., 2015), so
332 do their distinct release strategies apply to both transmitters? Our anatomical approach reliably
333 detects GABA presynaptic sites, with a high percentage of co-localisation between synaptophysin-
334 mRuby and vGAT (**Figure 1**). However, not all synaptophysin-mRuby puncta are vGAT-positive. This
335 could reflect technical limitations in release site detection (Risher et al., 2015; Heise et al., 2016), but
336 also indicates that vGAT-negative spots may represent specific dopamine release sites (Borisovska et
337 al., 2013; Liu et al., 2013; Vaaga et al., 2017). Indeed, in other brain regions synaptophysin-mRuby
338 puncta have been used to reveal sites of dopamine release (Li et al., 2005). In OB DA neurons GABA
339 and dopamine release are associated with different functions (Lyons-Warren et al., 2023) and the
340 two transmitters are known not to be released from the same vesicles (Borisovska et al., 2013).
341 However, this does not necessarily imply that they are released from different active zones.
342 Addressing this question in the current study was unfortunately not possible due to notorious
343 difficulties in staining the dopamine vesicular transporter 2 (VMAT2; Zhang et al., 2015; Jain et al.,
344 2023). Whether anaxonic and axon-bearing DA neurons release dopamine and GABA from the same
345 sites remains an important question for future studies.

346 In light of our findings, many fascinating questions about anaxonic DA neurons remain to be
347 explored. How is dendritic release developed and maintained throughout the life of the neuron?
348 Specific mechanisms have been identified that drive the establishment and maintenance of neuronal
349 polarity in neurons with a classic axodendritic configuration (for reviews see Rasband, 2010; Lalli,
350 2014; Bentley and Banker, 2016). Do some of these molecular events, like cytoskeleton
351 reorganisation and/or trafficking processes, differ in the dendrites of anaxonic neurons versus the
352 'standard' dendrites of axon-bearing neurons? Future work will answer these and further questions
353 on the developmental and functional intricacies of unconventional neurons in the brain.

354

355 **Does dendritic release equal self-inhibition?**

356

357 Self-inhibition in the olfactory bulb was initially discovered in a subset of periglomerular cells (Smith
358 and Jahr, 2002) and later described specifically in dopaminergic neurons (Maher and Westbrook,
359 2008). Here, we find that self-inhibition is not a universal OB DA neuron feature, but instead is an
360 almost exclusive property of anaxonic DA cells. By ruling out potential external sources of GABA in
361 the glomerular circuit, we have also provided the clearest evidence to date for true self-inhibition in
362 OB periglomerular cells.

363 The link between dendritic release of neurotransmitters and self-inhibition exists in other brain
364 regions as well. Neurons in the substantia nigra release dopamine that binds to auto-receptors and
365 subsequently inhibits the neuron (Pucak and Grace, 1994; Falkenburger et al., 2001). Other examples
366 include noradrenergic neurons in the locus coeruleus and serotonergic cells in the nucleus raphe
367 dorsalis (Aghajanian et al., 1977; Liu et al., 2005). However, while these neurons have a classic
368 axodendritic polarity and are able to release from their axons as well, anaxonic DA cells constitute a
369 distinct model as dendrites are the solely available compartment for such function.

370 Finally, does dopamine released from an anaxonic OB DA neuron also modulate that same neuron?
371 Our own data demonstrate that the auto-evoked inhibition current is purely GABAergic: it is
372 suppressed after the application of gabazine, but unaffected after blocking dopamine receptors
373 (**Figure 5**). In addition, our transcriptomic data clearly show that OB DA neurons do not express
374 dopamine receptors at all (**Figure 4**). It is therefore unlikely there is a dopaminergic component to

375 the self-inhibition response. Previous reports of dopamine-driven responses in OB DA neurons (Liu,
376 2020) may instead have occurred via well-described gap junction connectivity between DA cells and
377 dopamine-responsive ETCs (Liu et al.2013; Banerjee et al., 2015).

378 **Implications for information processing**

379 Anaxonic DA neurons release neurotransmitters from their dendrites, which are confined to local
380 areas of the glomerular layer. In contrast, axon-bearing DA cells release from their axons, which
381 spread for long distances across the glomerular layer (Kosaka and Kosaka, 2008; Galliano et al.,
382 2018). Our findings lead to the prediction of a clear division of circuit function for very closely related
383 cell subtypes: anaxonic DA neurons take part in local, intraglomerular inhibition, while axon-bearing
384 DA cells participate in distal, interglomerular inhibition.

385 Functionally, intraglomerular inhibition acts as 'high pass filter' for weak odour signals detected in a
386 glomerulus, enhancing the contrast between different olfactory stimuli (Shao et al., 2012; Gire and
387 Schoppa, 2009; Zak and Schoppa, 2021). Anaxonic DA neurons are therefore expected to contribute
388 to intraglomerular inhibition via different pathways which have been generally described for
389 periglomerular cells. This includes the exclusively intraglomerular presynaptic inhibition of olfactory
390 sensory neurons (Hsia et al., 1999; Ennis et al., 2001; McGann et al., 2005; Korshunov et al., 2017;
391 McGann 2013; Vaaga et al., 2017**;**), as well as the dendrodendritic inhibition of multiple
392 neighbouring glomerular cell types, including interneurons and projection neurons (Murphy et al.,
393 2005; Gire and Schoppa, 2009).

394 Self-inhibition would be expected to decrease the capacity of anaxonic DA neurons to release GABA
395 over time, therefore reducing inhibitory influence within glomerular circuits. Self-inhibition could
396 therefore control the timing of intraglomerular inhibition, allowing subsequent stimuli to activate
397 glomerular networks. Self-inhibition could also aid the high-pass filter function of glomerular
398 networks (Gire and Schoppa, 2009). If it occurs exclusively in the context of strong DA neuron
399 activation, it could decrease intraglomerular inhibition to promote glomerular output when input
400 strength goes past a certain threshold. There is also the possibility that self-inhibition is more of a
401 bug than a feature. Perhaps if anaxonic DA neurons have to release GABA from their dendrites in
402 order to perform their intraglomerular circuit functions, the chances are high that their nearby
403 postsynaptic receptors cannot escape some of that GABAergic influence. Further work is needed to
404 investigate how these mechanisms influence overall intraglomerular inhibition and glomerular
405 output.

406 Glomeruli in the olfactory bulb create a spatial map of odour identity, where different odours
407 specifically activate different combinations of glomeruli (Soucy et al., 2009; Murthy, 2011).
408 Interglomerular inhibition acting between different glomeruli selectively enhances the signal
409 contrast in between individual stimuli, boosting odour identification and/or discrimination (Uchida
410 et al., 2000; Urban, 2002). This circuit function must be exclusively undertaken by axon-bearing DA
411 neurons, due to their unique capacity for long-range axonal release of neurotransmitters (this paper,
412 Liu et al., 2013; Whitesell et al., 2013; Banerjee et al., 2015).

413 Several key traits are shared across the entire population of OB DA neurons, including their
414 dopaminergic and GABAergic identities and their glomerular location in the olfactory circuitry.
415 Despite these similarities, we have found fundamental differences between OB DA subtypes in terms
416 of their anatomy, neurotransmitter release compartments and the presence/absence of self-
417 inhibition. These are strong foundations to suggest entirely different sensory processing functions in
418 even very closely related interneuron sub-populations.

419

420

421 ## Materials and Methods

422 ### Animals

423 We used mice of either sex and housed them under a 12h light-dark cycle in an environmentally
424 controlled room with access to water and food *ad libitum*. Wild-type C57/Bl6 mice (Charles River)
425 were used either as experimental animals, or to back-cross each generation of transgenic animals.
426 The founders of our transgenic mouse lines – vGAT-Cre (Slc32a1$^{tm2(cre)Lowl}$/J, Jax stock 016962), DAT-
427 Cre (B6.SJL-Slc6a3$^{tm1.1(cre)Bkmn}$/J, Jax stock 006660) and flex-tdTomato (B6.Cg–Gt(ROSA)26Sor$^{tm9(CAG-}$
428 $^{tdTomato)Hze}$/J , Jax stock 007909) were purchased from The Jackson Laboratory. Immunohistochemistry
429 experiments with vGAT-Cre mice were performed at postnatal day (P)28. Patch-clamp
430 electrophysiology experiments with DAT-tdT mice were performed between P21-P35. All
431 experiments were performed in accordance with the United Kingdom Animals (Scientific Procedures)
432 Act 1986, under the auspices of Home Office personal and project licenses held by the authors.

433

434 ### Viral injections

435 To sparsely label neuronal morphology together with presynaptic release sites, vGAT-Cre mice were
436 injected *in utero* via intraventricular injection with AAV-DJ-hSyn-FLEx-mGFP-T2A-Synaptophysin-
437 mRuby (3 x 10^{12} GC/ml, AAV DJ GVVC-AAV-100, Stanford Vector Core Facility) (Beier et al., 2015;
438 Kathe et al., 2022) at embryonic day (E)14. Time-mated pregnant mice were anaesthetised with
439 isoflurane, used at 4% for general anaesthesia induction and at 2% for anaesthesia maintenance.
440 Injections (≈1µl) were performed with a glass-pulled pipette (1B150-F4, World Precision
441 Instruments) through the uterine wall into one of the lateral ventricles of the embryos. The uterine
442 horns were then returned into the abdominal cavity, the wall and the skin were sutured, and the
443 embryos were allowed to continue their development *in utero* and born naturally until experimental
444 use. Post-surgery, mice recovered in a 32°C chamber and were housed individually.

445

446 ### Immunohistochemistry

447 P28 and P33 mice were anaesthetised with an overdose of pentobarbital and then perfused with 20-
448 25 ml of PBS with heparin (A16198, Thermo Fisher Scientific) (20 units/mL), followed by 20-25 ml of
449 4% paraformaldehyde (PFA; P001, TAAB Laboratories) in 3% sucrose, 60 mM PIPES, 25 mM HEPES, 5
450 mM EGTA, and 1 mM $MgCl_2$ (all purchased from Sigma-Aldrich). The olfactory bulbs were dissected
451 and post-fixed in 4% PFA overnight (4°C), then embedded in 5% agarose and sliced at 50 µm using a
452 vibratome (VT1000S, Leica). Free-floating slices were washed with PBS 1x and permeabilised and
453 blocked in PBS with 5% normal goat serum (NGS, G9023, Sigma-Aldrich) and 0.25% Triton (Triton
454 X100, Sigma-Aldrich) for 2 hr at room temperature (RT). Slices were then incubated in primary
455 antibody solution (antibodies diluted in PBS with 5% and 0.25% Triton) for 2-5 days at 4°C. Primary
456 antibodies, working dilutions and sources are indicated in Table 1. Slices were then washed three
457 times for 10 minutes with PBS, before being incubated in secondary antibody solution (species-
458 appropriate Life Technologies Alexa Fluor-conjugated; all at a 1:1000 dilution in PBS with 5% NGS
459 and 0.25% Triton) for 2h at RT. After washing 3 times for 10 minutes with PBS, slices were mounted
460 on glass slides (J2800AMNZ, Epredia) with FluorSave (345789, Merck).

461 All immunostainings involving multiple targets were performed by incubating the primary antibodies
462 simultaneously, except for the combination of mouse anti-TH and rat anti-MBP, where a sequential
463 incubation was necessary to avoid cross-reactivity (first TH, then MBP).

464 *Table 1. Primary antibodies.*

Target	Host	Dilution	Supplier	Reference	Identifier
TH	Mouse	1/500, 1/5000, 1/10000 and 1/50000	Merck	MAB318	RRID:AB_2201528
GFP	Chicken	1/1000	Abcam	ab13970	RRID:AB_300798
TRIM46	Guinea pig	1/500	Synaptic Systems	377005	RRID:AB_2721101
mCherry	Rat	1/500	Thermo Fisher	M11217	RRID:AB_2536611
vGAT	Rabbit	1/1000	Synaptic Systems	131002	RRID:AB_887871
MBP	Rabbit	1/1000	Thermo Fisher	PA5-78397	RRID:AB_2736178
MBP	Rat	1/500	Millipore	MAB386	RRID:AB_94975
Gephyrin	Rabbit	1/500	Synaptic Systems	147008	RRID:AB_2619834
Synaptophysin	Guinea pig	1/500	Synaptic Systems	101004	RRID:AB_1210382

465

466

467 **Image acquisition, analysis, and illustration**

468 *Acquisition*

469 All images were acquired using a laser scanning confocal microscope (Zeiss LSM 710, equipped with
470 Zen 2010 B-SP1 software) using appropriate excitation and emission filters, a pinhole of 1 AU and
471 40x or 63x oil immersion objectives. Laser power and gain were set to prevent fluorescence
472 saturation and allow acquisition with an optimal signal-to-noise ratio, and z-stacks were acquired at
473 software-defined optimal thickness and step sizes. For puncta detection and dendritic
474 reconstruction, stacks were acquired with 1x zoom (0.033 μm/pixel), 2048 x 2048 pixels, and in z-
475 stacks with 0.37 μm steps. The dopaminergic identity of the cells was assessed qualitatively by taking
476 a single plane snapshot of the TH and GFP channels that included the soma. Axon-bearing neurons
477 displayed at least one clear elongated TRIM46-positive region (of approximately 10 to 25 μm in
478 length) that belonged to a GFP+ process. For co-localisation analyses, stacks were acquired with 2x
479 zoom (0.033 μm/pixel), 2048 x 2048 pixels, and in z-stacks with 0.37 μm steps. Due to the low
480 penetration of the vGAT antibody, and following similar studies (Heise et al., 2016), these stacks
481 were thinner (1.1-1.2 μm total depth) to capture most of the signal and perform reliable co-
482 localisation assessment.

483

484 *Analysis*

485 Puncta detection and dendritic tracing in 3D stacks were performed using Imaris (version 9.1.2).
486 Synaptophysin-mRuby belonging to specific GFP processes were detected based on their signal
487 overlap with GFP. To automate puncta detection, synaptophysin-mRuby and gephyrin puncta were
488 detected by estimating a punctum size of 0.5 μm and then using the 'Quality' filter. Detection
489 threshold was kept within an unbiased consistent range (1000 to 2700) that allowed adaptation to
490 variability between staining experiments and mice. Dendritic traces were performed using the
491 'Filaments' function, and the total length and maximum length of dendrites were calculated
492 accordingly. Puncta density was estimated by dividing the total number of puncta by the total length
493 of dendrites.

494 For co-localisation analysis, the 3-dimensional centroid coordinates for the synaptophysin-mRuby
495 puncta detected in Imaris were exported and analysed using a custom-written script in Matlab. This
496 determined, at the y- and z-axis centroid co-ordinates of each mRuby punctum, the vGAT

497 fluorescence intensity averaged over a 1 µm window centred on the local maximum of the mRuby
498 distribution's x-position. If this mRuby-centred vGAT fluorescence intensity was greater than 1
499 standard deviation higher than local background vGAT fluorescence (taken from a 1 µm window
500 immediately outside the x-axis border of the mRuby punctum), the punctum was considered to be
501 'co-localised.' The overall percentage of co-localised puncta was then determined for each cell.

502 For soma size measurements, 3D stacks were first transformed into maximum intensity projections.
503 We used the polygon drawing tool on Fiji (Schindelin et al., 2012) to draw the soma and obtained the
504 area measurements using the 'measure' function.

505

506 *Illustration*

507 All images in the manuscript displaying examples of immunostaining were taken as high-resolution
508 snapshots on ImarisViewer (version 10.2.0). Image stitching in Figure 3 was performed using
509 maximum intensity projections of individual stacks that were assembled using the ImageJ plugin
510 MosaicJ (Thevenaz and Unser, 2007). Orthogonal views in Figure 1F were created in Fiji (Schindelin
511 et al., 2012). Schematics, drawings, and figures layouts were designed using Inkscape (version 1.3.2).

512

513 **Acute slice preparation**

514 DAT-tdTomato mice at P21-35 were decapitated under isoflurane anaesthesia, and the olfactory
515 bulb was removed and transferred into ice-cold slicing medium containing (in mM): 240 sucrose, 5
516 KCl, 1.25 Na_2HPO_4, 2 $MgSO_4$, 1 $CaCl_2$, 26 $NaHCO_3$ and 10 D-Glucose (all reagents from Sigma-Aldrich),
517 bubbled with 95% O_2 and 5% CO_2. Horizontal slices (300 µm) of the olfactory bulb were cut using a
518 vibratome (VT1000S, Leica and 7000 smz-2, Campden Instruments) and maintained in artificial
519 cerebrospinal fluid (ACSF) containing (in mM): 124 NaCl, 2.5 KCl, 1.25 Na_2HPO_4, 2 $MgSO_4$, 2 $CaCl_2$, 26
520 $NaHCO_3$ and 15 D-Glucose, bubbled with 95% O_2 and 5% CO_2. Slices were kept for 30 minutes in a
521 water bath at 34 ^oC and then left to recover for 30 minutes at room temperature (RT).

522

523 **Acute slice electrophysiology**

524 Individual slices were placed in a chamber mounted on a FN1 Fixed Stage Nikon microscope and held
525 in place with a stainless-steel slice anchor. Slices were continuously superfused with ACSF heated to
526 physiologically relevant temperature (34 ± 1^oC) using an in-line solution heater (TC-344B, Warner
527 Instruments). The ACSF contained, at all times, the NMDA receptor blocker DL-2-Amino-5-
528 phosphonopentanoic acid at 50 µM (APV; A5282, Sigma-Aldrich), the AMPA receptor blocker 2,3-
529 dioxo-6-nitro-7-sulfamoyl-benzo[f]quinoxaline at 10 µM] (NBQX; N183, Sigma-Aldrich). The sodium
530 channel blocking tetrodoxin citrate (TTX; T-550, Alomone and 1069, Tocris) was used at 10 µM for all
531 experiments excluding action potential recordings. Block of GABA-A receptors was achieved by the
532 application of SR-95531 gabazine (1262, Tocris) for 5 minutes in the bath at 10 µM and confirmed by
533 the absence of IPSCs. D1-like and D2-like receptors were blocked by applying SFK 83566
534 hydrobromide for 5 minutes in the bath at 10 µM (1586, Tocris) and sulpiride at 10 µM (S8010,
535 Sigma-Aldrich), respectively. Calcium channels were blocked by applying cadmium chloride (202908,
536 Sigma) at 200 µM for 5 minutes in the bath. The gap junction blocker carbenoxolone disodium at 100
537 µM (3096, Tocris) and the NKCC1 blocker bumetanide at 20 µM (3108, Tocris) were applied in the
538 bath from the beginning and kept in the ACSF for at least 20-40 minutes. We adopted this strategy

539 due to two key considerations: (1) carbenoxolone induced instability in the membrane properties of
540 the neurons during the initial minutes of application, and (2) sufficient time was required for
541 chloride transporters to reach a steady intracellular chloride concentration ([Cl^-]) in response to
542 bumetanide.

543 Recording pipettes were pulled from borosilicate glass (1B150F-4, World Precision Instruments) with
544 a vertical puller (PC-10, Narishige). Some were tip fire-polished with a microforge (MF-830,
545 Narishige). All auto-evoked inhibition (AEI) recordings were performed using Caesium Chloride
546 intracellular solution (in mM: 125 CsCl, 10 HEPES, 0.1 EGTA, 4 MgATP, 0.3 Na_3GTP, 10
547 phosphocreatine, 10 GABA (280-290 mOsm and pHed to ~7.3 with CsOH), and pipette resistances of
548 2-4 MΩ.

549

550 *Auto-evoked inhibition recordings in non-injected mice*

551 DAT-tdTomato neurons were visualised with a 40x water immersion objective and tdTomato
552 fluorescence was revealed by LED excitation (CoolLED pE-100) with appropriate excitation and
553 emission filters. Recordings were performed using a HEKA EPC 10/2 amplifier coupled to
554 PatchMaster acquisition software (HEKA Elektronik). Signals were digitised and sampled at 20 kHz
555 (50 µs interval sample) unless otherwise stated, and Bessel filtered at 10 kHz (filter 1) and 2.9 kHz
556 (filter 2).

557 Axon-bearing and anaxonic DA neurons were identified based on their action potential waveform.
558 For that, cells were held at -60 mV in current clamp with 100% bridge balance. 10 ms somatic
559 current injections of Δ+5 pA steps were applied until threshold was reached and an action potential
560 occurred. 10 ms duration current injections were sampled at high temporal resolution 200 kHz (5 µs
561 sample interval) and the recordings were smoothed prior to differentiation using a 20 point (100 µs)
562 sliding filter. The first derivative of the smoothed trace was used for dV/dt and phase plane plot
563 analyses. Neurons were then visually determined as axon-bearing or anaxonic based on their
564 biphasic or monophasic phase plane plot profiles, respectively (Galliano et al., 2018).

565 Spontaneous IPSCs were recorded as inward events at –80 mV for 1 minute while 1 µM TTX was
566 added to the ACSF. Sodium channel block was confirmed by running an IV protocol and observing
567 the block of the large, inward sodium current.

568 AEI recordings were sampled at 50 kHz (20 µs sample interval), with slow capacitance compensated.
569 After membrane rupture, a test series was performed. Series resistance (R_S), calculated from the
570 peak current, was assessed continuously and recordings were excluded if they exceeded 30 MΩ at
571 any point or changed more 30% during any recording. AEI protocols were performed in voltage-
572 clamp from a holding potential of –80 mV, unless otherwise stated. Neurons were depolarised to 0
573 mV for 10 or 100 ms, before returning to –80 mV. Paired recordings were two 10 ms duration
574 voltage steps with 50 ms inter-stimulus interval. All protocols were repeated 3 times, with 30
575 seconds in between each sweep, and an average response calculated. Due to the presence of
576 passive currents, sweeps were analysed from 10 ms after the end of the voltage step for 500 ms.
577 Gabazine and cadmium-sensitive AEI currents were measured as the difference between the pre-
578 and the post-treatment averaged traces. The final charge was calculated as the area under the curve
579 of the subtracted response.

580 We confirmed no change in the AEI response over time by repeating the 10 ms voltage step protocol
581 3 times, with 5 minutes in between each protocol. No significant change in the charge of the AEI

582 response was found during the experiment (mean ± SEM: timepoint 1, 25 ± 7.99 pC; timepoint 2,
583 27.29 ± 9.57 pC; timepoint 3, 29.29 ± 11.22 pC; n = 5, N = 4 mice; one-way repeated measures
584 ANOVA, p = 0.44). We also ruled out the effect of somatic depolarisation on the AEI response by
585 holding the DA neurons either at -50 mV or -80 mV for approximately 30 seconds before the start of
586 the recordings. Neurons were then depolarised to 0 mV for 10 ms and then brought to -80 mV. The
587 AEI response was not different between holding at -50 mV or -80 mV (mean ± SEM: -50 mV
588 response, 25.45 ± 4.53 pC; -80 mV response, 25.3 ± 7.3 pC; n = 5, N = 3 mice, paired t-test, p = 0.96).
589 These results suggest that our experimental design produces a reliable and stable response to study
590 auto-evoked inhibition in this neuronal population.

591

592 **Data analysis**

593 For RNAseq data plotting, we made use of a single cell RNAseq dataset derived from whole olfactory
594 bulb, subsetting and plotting only the dopaminergic neurons (Brann et al., 2020). Violin plots
595 depicting the expression of *Th* (tyrosine hydroxylase), *Syp* (synaptophysin) and *Drd1* and *Drd2*
596 (dopamine receptors 1 and 2), in the cell cluster corresponding to the dopaminergic neurons, were
597 generated with the R package Seurat.

598 Overall, data analysis, statistical analysis and plotting were carried out using GraphPad (San Diego,
599 CA), R and custom-written Matlab (Mathworks) scripts. Data are reported as mean ± SEM unless
600 otherwise stated. 'N' represents the number of mice and 'n' is the number of cells. Details of
601 individual statistical tests can be found in the results section and in figure legends. Data sets were
602 tested for normality using the D'Agostino and Pearson tests where the datasets were sufficiently
603 large, and Shapiro-Wilk test if not. Statistical tests were determined considering the distribution of
604 the data (normal or non-normal) and sample variance (equal or unequal). All tests were two-tailed,
605 with $\alpha = 0.05$.

606

607 **Data availability statement**

608 The full raw dataset supporting this article will be openly available upon manuscript acceptance in a
609 peer-reviewed journal at the King's College London research repository (reserved DOI:
610 10.18742/27731157).

611

612 **Author contributions**

613 DJB and MSG designed experiments; AD-R, DJB, YL, MC, CA and MCF performed experiments; AD-R,
614 DJB, YL, ML and MSG analysed data, AD-R and MSG wrote the paper.

615

616 **Acknowledgements**

617 This work was supported by a Wellcome Trust Early-Career Award to AD-R and MSG
618 (227621/Z/23/Z); BBSRC Research Grants (BB/V000195/1 and BB/N014650/1) and an H2020 ERC
619 Consolidator Grant (FUNCOPLAN; 725729) to MSG; and an MRC Medical Research Council 4-year
620 PhD studentship to DJB. We thank Elisa Galliano for valuable comments on the manuscript, the
621 Andreae lab and the Centre for Developmental Neurobiology for image analysis support, Ikhlas

Kechround and Nadine Leighton for immunostaining optimisation, the Burrone lab for advice on presynaptic labelling, Candida Tufo and Lorcan Browne for guidance and training in patch-clamp electrophysiology and the current members of the Grubb lab for insightful discussions throughout the project.

References

Aghajanian, G.K., Cedarbaum, J.M., Wang, R.Y., 1977. Evidence for norepinephrine-mediated collateral inhibition of locus coeruleus neurons. Brain Research 136, 570–577. https://doi.org/10.1016/0006-8993(77)90083-X

Bäckman, C.M., Malik, N., Zhang, Y., Shan, L., Grinberg, A., Hoffer, B.J., Westphal, H., Tomac, A.C., 2006. Characterization of a mouse strain expressing Cre recombinase from the 3' untranslated region of the dopamine transporter locus. genesis 44, 383–390. https://doi.org/10.1002/dvg.20228

Banerjee, A., Marbach, F., Anselmi, F., Koh, M.S., Davis, M.B., Garcia da Silva, P., Delevich, K., Oyibo, H.K., Gupta, P., Li, B., Albeanu, D.F., 2015. An Interglomerular Circuit Gates Glomerular Output and Implements Gain Control in the Mouse Olfactory Bulb. Neuron 87, 193–207. https://doi.org/10.1016/j.neuron.2015.06.019

Banker, G., 2018. The Development of Neuronal Polarity: A Retrospective View. J. Neurosci. 38, 1867–1873. https://doi.org/10.1523/JNEUROSCI.1372-16.2018

Batista-Brito, R., Close, J., Machold, R., Fishell, G., 2008. The Distinct Temporal Origins of Olfactory Bulb Interneuron Subtypes. J. Neurosci. 28, 3966–3975. https://doi.org/10.1523/JNEUROSCI.5625-07.2008

Beier, K.T., Steinberg, E.E., Deloach, K.E., Xie, S., Miyamachi, K., Schwarz, L., Gao, X.J., Kremer, E.J., Malenka, R.C., Luo, L., 2015. Circuit architecture of VTA dopamine neurons revealed by systematic input-output mapping. Cell, 162(3), 622–634. https://doi.org/10.1016/j.cell.2015.07.015.

Bentley, M., Banker, G., 2016. The cellular mechanisms that maintain neuronal polarity. Nat Rev Neurosci 17, 611–622. https://doi.org/10.1038/nrn.2016.100

Berkowicz, D.A., Trombley, P.Q., 2000. Dopaminergic modulation at the olfactory nerve synapse. Brain Research 855, 90–99. https://doi.org/10.1016/S0006-8993(99)02342-2

Borisovska, M., Bensen, A.L., Chong, G., Westbrook, G.L., 2013. Distinct Modes of Dopamine and GABA Release in a Dual Transmitter Neuron. J. Neurosci. 33, 1790–1796. https://doi.org/10.1523/JNEUROSCI.4342-12.2013

Bouhours, Brice, Federico F. Trigo, and Alain Marty. 2011. 'Somatic Depolarization Enhances GABA Release in Cerebellar Interneurons via a Calcium/Protein Kinase C Pathway'. *Journal of Neuroscience* 31 (15): 5804–15. https://doi.org/10.1523/JNEUROSCI.5127-10.2011.

Brann, D.H., Tsukahara, T., Weinreb, C., Lipovsek, M., Van den Berge, K., Gong, B., Chance, R., Macaulay, I.C., Chou, H.-J., Fletcher, R.B., Das, D., Street, K., de Bezieux, H.R., Choi, Y.-G., Risso, D., Dudoit, S., Purdom, E., Mill, J., Hachem, R.A., Matsunami, H., Logan, D.W., Goldstein, B.J., Grubb, M.S., Ngai, J., Datta, S.R., 2020. Non-neuronal expression of SARS-CoV-2 entry genes in the olfactory system suggests mechanisms underlying COVID-19-associated anosmia. Science Advances 6, eabc5801. https://doi.org/10.1126/sciadv.abc5801

662 Castro, J.B., Urban, N.N., 2009. Subthreshold Glutamate Release from Mitral Cell Dendrites. J.
663 Neurosci. 29, 7023–7030. https://doi.org/10.1523/JNEUROSCI.5606-08.2009

664 Chand, A.N., Galliano, E., Chesters, R.A., Grubb, M.S., 2015. A Distinct Subtype of Dopaminergic
665 Interneuron Displays Inverted Structural Plasticity at the Axon Initial Segment. J. Neurosci. 35, 1573–
666 1590. https://doi.org/10.1523/JNEUROSCI.3515-14.2015

667 Cheramy, A., Leviel, V., Glowinski, J., 1981. Dendritic release of dopamine in the substantia nigra.
668 Nature 289, 537–542. https://doi.org/10.1038/289537a0

669 Coronas, V., Srivastava, L.K., Liang, J.-J., Jourdan, F., Moyse, E., 1997. Identification and localization
670 of dopamine receptor subtypes in rat olfactory mucosa and bulb: a combined in situ hybridization
671 and ligand binding radioautographic approach. Journal of Chemical Neuroanatomy 12, 243–257.
672 https://doi.org/10.1016/S0891-0618(97)00215-9

673 Ennis, M., Zhou, F.-M., Ciombor, K.J., Aroniadou-Anderjaska, V., Hayar, A., Borrelli, E., Zimmer, L.A.,
674 Margolis, F., Shipley, M.T., 2001. Dopamine D2 Receptor–Mediated Presynaptic Inhibition of
675 Olfactory Nerve Terminals. Journal of Neurophysiology 86, 2986–2997.
676 https://doi.org/10.1152/jn.2001.86.6.2986

677 Falkenburger, B.H., Barstow, K.L., Mintz, I.M., 2001. Dendrodendritic Inhibition Through Reversal of
678 Dopamine Transport. Science 293, 2465–2470. https://doi.org/10.1126/science.1060645

679 Galliano, E., Franzoni, E., Breton, M., Chand, A.N., Byrne, D.J., Murthy, V.N., Grubb, M.S., 2018.
680 Embryonic and postnatal neurogenesis produce functionally distinct subclasses of dopaminergic
681 neuron. eLife 7, e32373. https://doi.org/10.7554/eLife.32373

682 Gire, D.H., Schoppa, N.E., 2009. Control of On/Off Glomerular Signaling by a Local GABAergic
683 Microcircuit in the Olfactory Bulb. J. Neurosci. 29, 13454–13464.
684 https://doi.org/10.1523/JNEUROSCI.2368-09.2009

685 Goaillard, J.-M., Moubarak, E., Tapia, M., Tell, F., 2020. Diversity of Axonal and Dendritic
686 Contributions to Neuronal Output. Frontiers in Cellular Neuroscience 13.

687 Granseth, B., Odermatt, B., Royle, S.J., Lagnado, L., 2006. Clathrin-Mediated Endocytosis Is the
688 Dominant Mechanism of Vesicle Retrieval at Hippocampal Synapses. Neuron 51, 773–786.
689 https://doi.org/10.1016/j.neuron.2006.08.029

690 Hayar, A., Karnup, S., Ennis, M., Shipley, M.T., 2004. External Tufted Cells: A Major Excitatory
691 Element That Coordinates Glomerular Activity. J. Neurosci. 24, 6676–6685.
692 https://doi.org/10.1523/JNEUROSCI.1367-04.2004

693 Heise, C., Schroeder, J.C., Schoen, M., Halbedl, S., Reim, D., Woelfle, S., Kreutz, M.R., Schmeisser,
694 M.J., Boeckers, T.M., 2016. Selective Localization of Shanks to VGLUT1-Positive Excitatory Synapses
695 in the Mouse Hippocampus. Frontiers in Cellular Neuroscience 10.

696 Hikima, T., Lee, C.R., Witkovsky, P., Chesler, J., Ichtchenko, K., Rice, M.E., 2021. Activity-dependent
697 somatodendritic dopamine release in the substantia nigra autoinhibits the releasing neuron. Cell
698 Reports 35. https://doi.org/10.1016/j.celrep.2021.108951

699 Hsia, A.Y., Vincent, J.-D., Lledo, P.-M., 1999. Dopamine Depresses Synaptic Inputs Into the Olfactory
700 Bulb. Journal of Neurophysiology 82, 1082–1085. https://doi.org/10.1152/jn.1999.82.2.1082

701 Imamura, F., Ito, A., LaFever, B.J., 2020. Subpopulations of Projection Neurons in the Olfactory Bulb.
702 Front. Neural Circuits 14. https://doi.org/10.3389/fncir.2020.561822

703 Isaacson, J.S., Strowbridge, B.W., 1998. Olfactory Reciprocal Synapses: Dendritic Signaling in the CNS.
704 Neuron 20, 749–761. https://doi.org/10.1016/S0896-6273(00)81013-2

705 Jain, S., Yee, A.G., Maas, J., Gierok, S., Xu, H., Stansil, J., Eriksen, J., Nelson, A.B., Silm, K., Ford, C.P.,
706 Edwards, R.H., 2023. Adaptor protein-3 produces synaptic vesicles that release phasic dopamine.
707 Proceedings of the National Academy of Sciences 120, e2309843120.
708 https://doi.org/10.1073/pnas.2309843120

709 Kathe, C., Skinnider, M.A., Hutson, T.H., Regazzi, N., Gautier, M., Demesmaeker, R., Komi, S., Ceto, S.,
710 James, N.D., Cho, N., Baud, L., Galan, K., Matson, K.J.E., Rowald, A., Kim, K., Wang, R., Minassian, K.,
711 Prior, J.O., Asboth, L., Barraud, Q., Lacour, S.P., Levine, A.J., Wagner, F., Bloch, J., Squair, J.W.,
712 Courtine, G., 2022. The neurons that restore walking after paralysis. Nature 611, 540–547.
713 https://doi.org/10.1038/s41586-022-05385-7

714 Kiyokage, E., Kobayashi, K., Toida, K., 2017. Spatial distribution of synapses on tyrosine hydroxylase–
715 expressing juxtaglomerular cells in the mouse olfactory glomerulus. Journal of Comparative
716 Neurology 525, 1059–1074. https://doi.org/10.1002/cne.24147

717 Korshunov, K.S., Blakemore, L.J., Trombley, P.Q., 2017. Dopamine: A Modulator of Circadian
718 Rhythms in the Central Nervous System. Front. Cell. Neurosci. 11.
719 https://doi.org/10.3389/fncel.2017.00091

720 Kosaka, T., Deans, M.R., Paul, D.L., Kosaka, K., 2005. Neuronal gap junctions in the mouse main
721 olfactory bulb: Morphological analyses on transgenic mice. Neuroscience 134, 757–769.
722 https://doi.org/10.1016/j.neuroscience.2005.04.057

723 Kosaka, T., Kosaka, K., 2008. Heterogeneity of parvalbumin-containing neurons in the mouse main
724 olfactory bulb, with special reference to short-axon cells and βIV-spectrin positive dendritic
725 segments. Neuroscience Research 60, 56–72. https://doi.org/10.1016/j.neures.2007.09.008

726 Lalli, G., 2014. Regulation of neuronal polarity. Experimental Cell Research, Cell polarity 328, 267–
727 275. https://doi.org/10.1016/j.yexcr.2014.07.033

728 Lau, M. Y. H., Gadiwalla, S., Jones, S., & Galliano, E., 2024. Different electrophysiological profiles of
729 genetically labelled dopaminergic neurons in the mouse midbrain and olfactory bulb. The European
730 journal of neuroscience, 59(7), 1480–1499. https://doi.org/10.1111/ejn.16239

731 Li, H., Waites, C.L., Staal, R.G., Dobryy, Y., Park, J., Sulzer, D.L., Edwards, R.H., 2005. Sorting of
732 Vesicular Monoamine Transporter 2 to the Regulated Secretory Pathway Confers the
733 Somatodendritic Exocytosis of Monoamines. Neuron 48, 619–633.
734 https://doi.org/10.1016/j.neuron.2005.09.033

735 Li, Y., Tsien, R.W., 2012. pHTomato, a red, genetically encoded indicator that enables multiplex
736 interrogation of synaptic activity. Nat Neurosci 15, 1047–1053. https://doi.org/10.1038/nn.3126

737 Liberia, T., Blasco-Ibáñez, J.M., Nácher, J., Varea, E., Zwafink, V., Crespo, C., 2012. Characterization of
738 a population of tyrosine hydroxylase-containing interneurons in the external plexiform layer of the
739 rat olfactory bulb. Neuroscience 217, 140–153. https://doi.org/10.1016/j.neuroscience.2012.05.007

740 Liu, R.-J., Lambe, E.K., Aghajanian, G.K., 2005. Somatodendritic autoreceptor regulation of
741 serotonergic neurons: dependence on L-tryptophan and tryptophan hydroxylase-activating kinases.
742 Eur J Neurosci 21, 945–958. https://doi.org/10.1111/j.1460-9568.2005.03930.x

743 Liu, S., 2020. Dopaminergic Modulation of Glomerular Circuits in the Mouse Olfactory Bulb. Front.
744 Cell. Neurosci. 14. https://doi.org/10.3389/fncel.2020.00172

745 Liu, S., Plachez, C., Shao, Z., Puche, A., Shipley, M.T., 2013. Olfactory Bulb Short Axon Cell Release of
746 GABA and Dopamine Produces a Temporally Biphasic Inhibition–Excitation Response in External
747 Tufted Cells. J. Neurosci. 33, 2916–2926. https://doi.org/10.1523/JNEUROSCI.3607-12.2013

748 Lyons-Warren, A.M., Tantry, E.K., Moss, E.H., Kochukov, M.Y., Belfort, B.D.W., Ortiz-Guzman, J.,
749 Freyberg, Z., Arenkiel, B.R., 2023. Co-transmitting interneurons in the mouse olfactory bulb regulate
750 olfactory detection and discrimination. Cell Reports 42, 113471.
751 https://doi.org/10.1016/j.celrep.2023.113471

752 Madisen, L., Zwingman, T.A., Sunkin, S.M., Oh, S.W., Zariwala, H.A., Gu, H., Ng, L.L., Palmiter, R.D.,
753 Hawrylycz, M.J., Jones, A.R., Lein, E.S., Zeng, H., 2010. A robust and high-throughput Cre reporting
754 and characterization system for the whole mouse brain. Nat Neurosci 13, 133–140.
755 https://doi.org/10.1038/nn.2467

756 Maher, B.J., Westbrook, G.L., 2008. Co-Transmission of Dopamine and GABA in Periglomerular Cells.
757 Journal of Neurophysiology 99, 1559–1564. https://doi.org/10.1152/jn.00636.2007

758 Marshak, D.W., 2016. A tale of two neurotransmitters. Visual Neuroscience 33, E017.
759 https://doi.org/10.1017/S0952523816000146

760 McGann, J.P., 2013. Presynaptic Inhibition of Olfactory Sensory Neurons: New Mechanisms and
761 Potential Functions. Chemical Senses 38, 459–474. https://doi.org/10.1093/chemse/bjt018

762 McGann, J.P., Pírez, N., Gainey, M.A., Muratore, C., Elias, A.S., Wachowiak, M., 2005. Odorant
763 Representations Are Modulated by Intra- but Not Interglomerular Presynaptic Inhibition of Olfactory
764 Sensory Neurons. Neuron 48, 1039–1053. https://doi.org/10.1016/j.neuron.2005.10.031

765 Murphy, G.J., Darcy, D.P., Isaacson, J.S., 2005. Intraglomerular inhibition: signaling mechanisms of an
766 olfactory microcircuit. Nat Neurosci 8, 354–364. https://doi.org/10.1038/nn1403

767 Murthy, V.N., 2011. Olfactory Maps in the Brain. Annu. Rev. Neurosci. 34, 233–258.
768 https://doi.org/10.1146/annurev-neuro-061010-113738

769 Nunes, D., Kuner, T., 2018. Axonal sodium channel NaV1.2 drives granule cell dendritic GABA release
770 and rapid odor discrimination. PLOS Biology 16, e2003816.
771 https://doi.org/10.1371/journal.pbio.2003816

772 Parsa, P.V., D'Souza, R.D., Vijayaraghavan, S., 2015. Signaling between periglomerular cells reveals a
773 bimodal role for GABA in modulating glomerular microcircuitry in the olfactory bulb. Proceedings of
774 the National Academy of Sciences 112, 9478–9483. https://doi.org/10.1073/pnas.1424406112

775 Pinching, A.J., Powell, T.P.S., 1971. The neuron types of the glomerular layer of the olfactory bulb.
776 Journal of Cell Science 9, 305–345. https://doi.org/10.1242/jcs.9.2.305

777 Pucak, M.L., Grace, A.A., 1994. Regulation of substantia nigra dopamine neurons. Crit Rev Neurobiol
778 9, 67–89.

Rasband, M.N., 2010. The axon initial segment and the maintenance of neuronal polarity. Nat Rev Neurosci 11, 552–562. https://doi.org/10.1038/nrn2852

Risher, M.-L., Sexton, H.G., Risher, W.C., Wilson, W.A., Fleming, R.L., Madison, R.D., Moore, S.D., Eroglu, C., Swartzwelder, H.S., 2015. Adolescent Intermittent Alcohol Exposure: Dysregulation of Thrombospondins and Synapse Formation are Associated with Decreased Neuronal Density in the Adult Hippocampus. Alcoholism: Clinical and Experimental Research 39, 2403–2413. https://doi.org/10.1111/acer.12913

Schindelin, J., Arganda-Carreras, I., Frise, E., Kaynig, V., Longair, M., Pietzsch, T., Preibisch, S., Rueden, C., Saalfeld, S., Schmid, B., Tinevez, J. Y., White, D. J., Hartenstein, V., Eliceiri, K., Tomancak, P., & Cardona, A., 2012. Fiji: an open-source platform for biological-image analysis. Nature Methods, 9(7), 676–682. https://doi.org/10.1038/nmeth.2019

Schoppa, N.E., Urban, N.N., 2003. Dendritic processing within olfactory bulb circuits. Trends in Neurosciences 26, 501–506. https://doi.org/10.1016/S0166-2236(03)00228-5

Schoppa, N.E., Westbrook, G.L., 2002. AMPA autoreceptors drive correlated spiking in olfactory bulb glomeruli. Nat Neurosci 5, 1194–1202. https://doi.org/10.1038/nn953

Shao, Z., Puche, A.C., Liu, S., Shipley, M.T., 2012. Intraglomerular inhibition shapes the strength and temporal structure of glomerular output. Journal of Neurophysiology 108, 782–793. https://doi.org/10.1152/jn.00119.2012

Smith, T.C., Jahr, C.E., 2002. Self-inhibition of olfactory bulb neurons. Nat Neurosci 5, 760–766. https://doi.org/10.1038/nn882

Soucy, E.R., Albeanu, D.F., Fantana, A.L., Murthy, V.N., Meister, M., 2009. Precision and diversity in an odor map on the olfactory bulb. Nat Neurosci 12, 210–220. https://doi.org/10.1038/nn.2262

Thévenaz, P., Unser, M., 2007. User-friendly semiautomated assembly of accurate image mosaics in microscopy. Microscopy Research and Technique 70, 135–146. https://doi.org/10.1002/jemt.20393

Tomassy, G.S., Berger, D.R., Chen, H.-H., Kasthuri, N., Hayworth, K.J., Vercelli, A., Seung, H.S., Lichtman, J.W., Arlotta, P., 2014. Distinct Profiles of Myelin Distribution Along Single Axons of Pyramidal Neurons in the Neocortex. Science 344, 319–324. https://doi.org/10.1126/science.1249766

Tufo, C., Poopalasundaram, S., Dorrego-Rivas, A., Ford, M.C., Graham, A., Grubb, M.S., 2022. Development of the mammalian main olfactory bulb. Development 149, dev200210. https://doi.org/10.1242/dev.200210

Uchida, N., Takahashi, Y.K., Tanifuji, M., Mori, K., 2000. Odor maps in the mammalian olfactory bulb: domain organization and odorant structural features. Nat Neurosci 3, 1035–1043. https://doi.org/10.1038/79857

Urban, N.N., 2002. Lateral inhibition in the olfactory bulb and in olfaction. Physiology & Behavior 77, 607–612. https://doi.org/10.1016/S0031-9384(02)00895-8

Vaaga, C.E., Yorgason, J.T., Williams, J.T., Westbrook, G.L., 2017. Presynaptic gain control by endogenous cotransmission of dopamine and GABA in the olfactory bulb. Journal of Neurophysiology 117, 1163–1170. https://doi.org/10.1152/jn.00694.2016

818 van Beuningen, S.F.B., Will, L., Harterink, M., Chazeau, A., van Battum, E.Y., Frias, C.P., Franker,
819 M.A.M., Katrukha, E.A., Stucchi, R., Vocking, K., Antunes, A.T., Slenders, L., Doulkeridou, S., Sillevis
820 Smitt, P., Altelaar, A.F.M., Post, J.A., Akhmanova, A., Pasterkamp, R.J., Kapitein, L.C., de Graaff, E.,
821 Hoogenraad, C.C., 2015. TRIM46 Controls Neuronal Polarity and Axon Specification by Driving the
822 Formation of Parallel Microtubule Arrays. Neuron 88, 1208–1226.
823 https://doi.org/10.1016/j.neuron.2015.11.012

824 Wachowiak, M., Cohen, L.B., 1999. Presynaptic Inhibition of Primary Olfactory Afferents Mediated by
825 Different Mechanisms in Lobster and Turtle. J. Neurosci. 19, 8808–8817.
826 https://doi.org/10.1523/JNEUROSCI.19-20-08808.1999

827 Whitesell, J.D., Sorensen, K.A., Jarvie, B.C., Hentges, S.T., Schoppa, N.E., 2013. Interglomerular
828 Lateral Inhibition Targeted on External Tufted Cells in the Olfactory Bulb. J. Neurosci. 33, 1552–1563.
829 https://doi.org/10.1523/JNEUROSCI.3410-12.2013

830 Wu, C., Ivanova, E., Cui, J., Lu, Q., Pan, Z.-H., 2011. Action Potential Generation at an Axon Initial
831 Segment-Like Process in the Axonless Retinal AII Amacrine Cell. J. Neurosci. 31, 14654–14659.
832 https://doi.org/10.1523/JNEUROSCI.1861-11.2011

833 Zak, J.D., Schoppa, N.E., 2022. Neurotransmitter regulation rather than cell-intrinsic properties
834 shapes the high-pass filtering properties of olfactory bulb glomeruli. The Journal of Physiology 600,
835 393–417. https://doi.org/10.1113/JP282374

836 Zhang, S., Qi, J., Li, X., Wang, H.-L., Britt, J.P., Hoffman, A.F., Bonci, A., Lupica, C.R., Morales, M.,
837 2015. Dopaminergic and glutamatergic microdomains in a subset of rodent mesoaccumbens axons.
838 Nat Neurosci 18, 386–392. https://doi.org/10.1038/nn.3945

839 Zilberter, Y., Kaiser, K.M.M., Sakmann, B., 1999. Dendritic GABA Release Depresses Excitatory
840 Transmission between Layer 2/3 Pyramidal and Bitufted Neurons in Rat Neocortex. Neuron 24, 979–
841 988. https://doi.org/10.1016/S0896-6273(00)81044-2

842

843

Supplementary figure 1

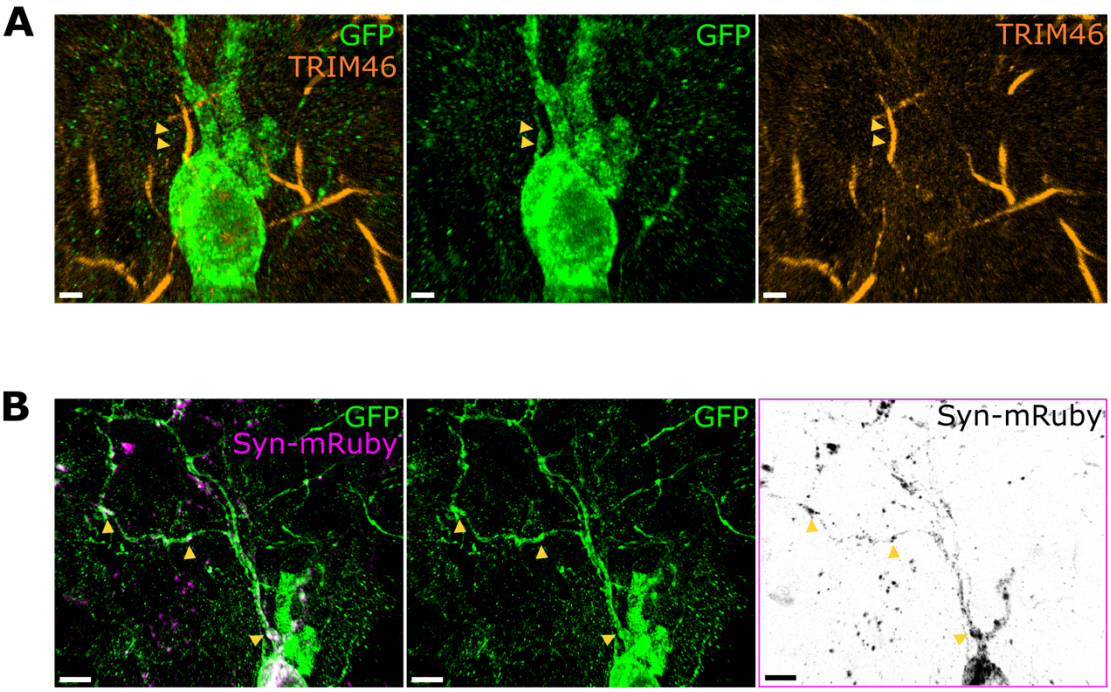

Supplementary figure 1. A single example of an axon-bearing DA neuron with potential dendritic release sites. (A) Snapshot of a 3D confocal stack of a DA neuron with GFP (green) and TRIM46 (orange) labelling, revealing the axon-bearing identity of the neuron. Yellow arrowheads point to the GFP+/TRIM46+ co-localised zone. Scalebars, 2 μm. **(B)** Snapshot of a 3D confocal stack showing synaptophysin-mRuby label (magenta, black) in the dendrites of the axon-bearing neuron from (A) (green). The levels of synaptophysin-mRuby look dramatically higher and with a less defined puncta profile than in all anaxonic DA cells – note levels of somatic expression compared to Figure 2B. Yellow arrowheads point to examples of detected puncta. Scalebars, 5 μm.